Materials and Design 164 (2019) 107560

Contents lists available at ScienceDirect

Materials and Design

journal homepage: www.elsevier.com/locate/matdes

Phononic dispersion in anisotropic pseudo-fractal hyper-lattices

A.S. Fallah [a,b,*], N. Navadeh [b], V.V. Tereshchuk [c], V.N. Gorshkov [c,d]

[a] Department of Mechanical Engineering, Howell Building, Brunel University London, Uxbridge, London UB8 3PH, UK
[b] Department of Aeronautics, City and Guilds Building, South Kensington Campus, Imperial College London, London SW7 2AZ, UK
[c] Department of Physics, Building 7, National Technical University of Ukraine (Igor Sikorsky Kyiv Polytechnic Institute), 37 Peremogy Avenue, Kiev-56 03056, Ukraine
[d] Theoretical Division, Los Alamos National Laboratory, Los Alamos, NM 87545, USA

HIGHLIGHTS

- Pseudo-fractal hyper-lattices are considered with dispersion surface morphology and frequency band structure being studied.
- Numerous dispersion surfaces form and eliminate bandgaps, a potentially useful feature for acoustic detectability.
- As a classical analogy to quantum level-repulsion, sound group velocity decreases, which is useful in many applications.
- The “rotating” and “displacing” modes correspond to separate wide frequency areas.
- A wide bandgap for displacing modes works as a pass-band for rotating modes and vice versa.

GRAPHICAL ABSTRACT

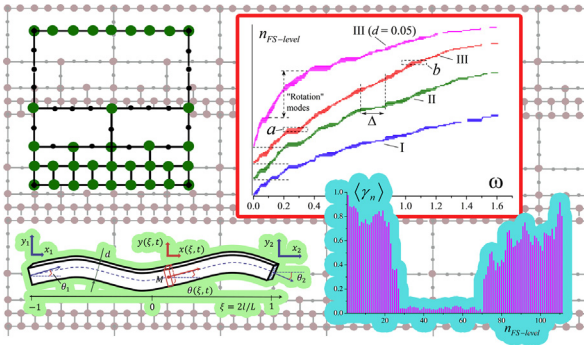

ARTICLE INFO

Article history:
Received 10 September 2018
Received in revised form 18 December 2018
Accepted 19 December 2018
Available online 22 December 2018

Keywords:
Fractals
Bandgap
Tailorability
Dispersion surface
Brillouin zone
Floquet-Bloch's principle

ABSTRACT

Fractal and pseudo-fractal microstructures have proved promising in increasing the range of detectable frequencies for devices used in the realm of electromagnetism. Due to mechanical-electrical duality it is conjectured they may provide flexible solutions capable of closing/widening bandgaps and increasing tailorability in phononic lattices. Pseudo-fractal hyper-lattices have been considered in this work and different aspects of dispersion surface morphology and frequency band structure are studied. It has been observed that higher frequencies that can be excited in the simple square lattice are almost the same as those in the pseudo-fractal structures, however; through introduction of higher levels the pseudo-fractal hyper-lattice presents new features not observable in the ordinary lattice. By increasing the order of pseudo-fractal structure the number of degrees-of-freedom increases and dispersion surfaces morphologies change thus frequency gaps are eliminated. This phenomenon can be of advantage for acoustic/phononic visibility/detectability e.g. in designing sensors. In the classical analogy to quantum level repulsion surfaces flatten which sufficiently decreases the sound group velocity in the pseudo-fractal structure, and can be used for numerous practical applications.

1. Introduction

Fractals are encountered time and again in nature. From rain forests where the distribution of length for branches in a single tree replicates, at a smaller scale, that of the height for trees in the forest to patterns of

* Corresponding author at: Department of Mechanical Engineering, Howell Building, Brunel University London, Uxbridge, London UB8 3PH, UK.
E-mail addresses: as3@imperial.ac.uk, mestasf@brunel.ac.uk (A.S. Fallah).

https://doi.org/10.1016/j.matdes.2018.107560

alluvial deposits subsequent to river formation where fractal ramification is encountered and from arrangement of healthy blood vessels in human body to geometry of vegetables, microstructure of lung airbags, fluid motion during cloud formation, occurrence of storm in weather systems, geometry of plants and flowers, pattern of heartbeats, spacing of noise in telecommunication, and scaling problems in animal kingdom. In all these cases fractals are solutions natural selection has come up with, but despite this fact, a satisfactory theory of fractal geometry was missing until the seminal works of Benoit Mandelbrot on the subject (see e.g. [1,2]). While the basic underlying principle is 'shrink the size and repeat' the resulting structure can be intricate enough to render it possible as the solution to a highly sophisticated nonlinear problem. If simple iterative procedures could provide the necessary solution, as the feedback loop could for the case of van Koch's snowflake [3] or in order to create the Mandelbrot set in the complex plane [4], it would be unnecessary to look for alternative solutions. Furthermore, it was shown in some cases fractals were not merely *a solution* but *the only solution* to a problem (see e.g. [5,6]).

These and other works in the field [7–10] led engineers in the direction of replicating nature and designing systems based on the fractal geometry. The revolution started in the field of electromagnetics and led to a breakthrough in telecommunication. Hohlfeld and Cohen [6] showed, for an antenna, fractals are the only solution to Maxwell's equations, a proposition which made mobile technology a theoretical possibility and subsequently a reality. The key finding was that not only could using fractals shrink the size but could make the antenna efficient in receiving signals of a wider spectrum of frequencies. This was essential in white noise detection as a very wide range of frequencies could be captured. First fractal antennas were successfully made and tested [10].

Given the mechanical-electrical analogy known for over a century (e.g. see Kron's extensive discussions of the topic ([11,12])) it is conjectured that fractal hyper-lattices are identified with unique characteristics, not readily available in unstructured media or ordinary lattices, and render it possible to increase the power of detection when mechanical waves of wide spectrum are concerned. While a solid medium can detect a wide range of frequencies there are two problems intrinsically involved for which an alternative solution must be sought: (1) a solid medium is much heavier than a fractal lattice and not suitable in weight-sensitive applications, and (2) there is no control over which frequencies must lie in the pass- or stop-bands for a solid medium. The weight/cost and tailorability issues may be solved through proposing a fractal or pseudo-fractal hyper-lattice.

The term 'hyper-lattice' is coined here to emphasise the fact that the internal micro-structure of the unit cell is a pseudo-fractal and possesses a structural arrangement comparable to that of a lattice, in itself. The proposed microstructure is not exactly a fractal (thus the prefix 'pseudo') as its dimension is not fractional (it is exactly 2 unlike a fractal which must possess a fractional dimension, as Sierpinski triangle which has the dimension of 1.585), however, it is generated through the same iterative procedures used to generate fractals (shrink and repeat). Furthermore, in the proposed arrangement each pseudo-fractal unit cell is repeated as its points are assigned to those of a substratum lattice. As phonons propagate through a latticed medium there are intervals of frequency over which the waves may not propagate. These are known as 'phononic bandgaps' or 'stopbands' and have been studied extensively by researchers in the field when analysing wave propagation in lattices [13–17] or phononic metamaterials [18–23]. As far as fractals are concerned, very few studies have been conducted on wave propagation in phononic fractals [24–28].

Theoretical and Computational studies in the field are limited, to mention a few that do deal with the problem, Song et al. [27] studied broadband fractal acoustic metamaterials for low-frequency sound attenuation. Low frequency sound attenuation in a subwavelength space is an interesting and challenging problem since the absorbers and the diffusers have to be thick enough to absorb or perturb the wave fronts due to the relatively long wavelengths. Their proposed fractal metamaterial provides a possible alternative for various applications such as noise attenuation and for anechoic materials. In another study, Ding et al. [26] looked into simultaneous realisation of slow and fast acoustic waves using the fractal structure of Koch curve. They designed an acoustic metamaterial based on a fractal structure, the Koch curve, to this end. Motivated by the encouraging results in the realm of electromagnetism and by the achievements in the control of electromagnetic waves and light, variant methods were adopted to manipulate the transmissions of acoustic waves. For instance, structures with labyrinthic or helical paths were used to slow down the propagations of acoustic waves on the basis of phase shifts originating from the transmissions along the curved and lengthened paths [29–34], which have exhibited their potential in sound blocking [30,31], directional sensing [32], broadband attenuation [33], and topological insulation [34]. Similar to labyrinthic structures, fractal structures, as the Koch curve [35,36], Sierpinski fractal [37,38], and Hilbert curve [39,40] were used to manipulate the transmissions of waves, which have been likewise widely adopted in electromagnetic metamaterials to obtain high impedance surfaces, broadband polarization, insensitive absorption, harmonic waves suppression, and directivity enhancement.

In another study, Song et al. [33] investigated a broadband focusing acoustic lens based on fractal metamaterials. Due to the self-similar properties of the proposed structure, broadband acoustic response may arise within a broad frequency range, making it a feasible candidate for a number of applications, such as super-resolution imaging and acoustic tunnelling. A flat acoustic lens was designed and experimentally verified using this approach, showing excellent focusing abilities for a range of frequencies between 2 kHz and 5 kHz of the measured results. Fractal labyrinthine acoustic metamaterial in planar lattices were studied by Liu et al. [34]. Through adapting the concept of Mie resonance of dielectric nanoparticle to the acoustic material, a new type of metamaterial, marked as the labyrinthine acoustic metamaterial, was developed (Christensen and Abajo [41], Liang and Li [42], Li et al. [43], Xie et al. [44], and Castiñeira-Ibáñez et al. [45]). In the labyrinthine acoustic metamaterial, the sound wave propagates along the zigzag channels but not along straight lines, thus the propagation length of the sound wave can be significantly multiplied depending on the angle of zigzag folding onto itself. In other words, compared to the background medium, the effective sound speed in the labyrinthine acoustic metamaterial is ultraslow. The labyrinthine acoustic metamaterials with ultraslow sound speed exhibit an extremely low absorption loss and a highly stable shape, which significantly extend our ability to control features of sound waves (such as the high reflection [41,42] and the negative refraction [43,44,46]). Acoustic metamaterials with fractal coiling up space for sound blocking in a deep subwavelength scale were studied by Xia et al. [44].

Recently, illuminated by fractal structures/composites, some hierarchical photonic/phononic crystals with fractal architectures have been investigated. Wen et al. [47] developed a series of planar conducting fractals with self-similar resonances to yield multiple bandgaps of electromagnetic waves. Chen et al. [48] proposed a microstrip filter with H-shaped fractals to produce multiple bandgaps and passbands of electromagnetic waves. Miyamaru et al. [49] demonstrated that H-shaped fractal structures presented a red shift in the resonant frequency with the increase of the fractal level. Hou et al. [50] fabricated a subwavelength photonic crystal using 3D metallic H-shaped fractals and investigated the hybridization between Bragg scattering and local resonance. Dupre et al. [51] proved that Hilbert fractal resonator alongside time reversal could be used to focus microwaves from a far field. Kuo and Piazza [52] experimentally verified that the fractal geometry could increase the operating frequency of the bandgap. Liu et al. [53] systematically investigated the effects of the T-shaped fractal holes on the band structure of a two-dimensional phononic crystal. Lim et al. [54] numerically and experimentally investigated the influence of fractal hierarchy on the transmission of elastic wave in a self-similar fractal beam lattice. Chen and Wang [55,56] investigated the propagation of elastic waves in

a bio-inspired hierarchical composite consisting of the hard mineral and the soft organic phases. Zhang and To [57] demonstrated that the bio-inspired hierarchical phononic crystal created wide bandgaps due to its intrinsic multiscale periodicities. Mousanezhad et al. [58] highlighted that the hierarchy of the two-dimensional fractal-like honeycomb phononic crystal could shift the first-order bandgap to lower frequencies.

In summary, these works suggest it is possible to create an acoustic metamaterial based on a fractal structure, such as the Koch curve, and establish a theoretical model to describe the acoustic transmission in the structure resembling an arbitrary order Koch curve. The structure may produce slow acoustic waves and fast waves even with negative group velocities on the basis of different physical mechanisms. Several related phenomena are conceivable, for instance, the resonance of the quasi-Koch-curve structure first traps the acoustic energy in the complex loop and creates a slow wave. Additionally, due to the destructive interference originating from acoustic waves travelling along different paths, a negative group velocity is realized. Therefore, multiple transmission paths for acoustic waves are produced based on one simple structure, and thus, diverse group velocities are achieved owing to the interaction of acoustic waves transmitting along different paths, which can be applied in the fields requiring the manipulation of acoustic transmissions.

In the present work, we first define the normalised geometry for a simple two-dimensional skeletal pseudo-fractal lattice unit cell (Section 2) and go on to define, based on this unit cell, the hyper-lattice structure. Then starting from the smallest element, the finite element model of the beam elements used in the model is formulated using the exact Timoshenko beam model thus the arbitrary n-th order pseudo-fractal hyper-lattice is exactly defined in Section 3. In Section 4 the lattice problem is formulated, the periodic boundary conditions (PBCs) are imposed on the unit cell and the eigenvalue problem is constructed using Floquet-Bloch's principle. Follow-up analyses are conducted to derive the dispersion surfaces for the phononic hyper-lattice in Section 5 and the dependencies on parameters are expounded. Since analytical solutions are derived for the case of $\boldsymbol{k} = 0$ (centre of the Brillouin zone (BZ)) the size of the gaps could be controlled using the dependencies on parameters defining the points of intersection of dispersion surfaces and the vertical frequency line. The study is concluded in Section 6.

2. The pseudo-fractal hyper-lattice structure

Considering a Bravais lattice in $\mathbb{R}^2$ its lattice points are generated in two dimensions using a single reference point and two linearly independent translation (direction) vectors. Subsequently the lattice points are assigned 'the basis' which comprises a set of elements that collectively characterise the unit cell of the lattice. In this way the entire lattice structure is thus constructed. In the present study the unit cell is assumed to be a square. The reasons for this choice are: (1) any rectangular unit cell can be simply mapped onto the square unit cell with a simple linear coordinate transformation, and (2) it was deduced, in a preliminary study, that the type of anisotropy due to different directional lattice constants is immaterial as far as the morphology of dispersion surfaces or bandgap widths are concerned. It is therefore sufficient to focus on the square unit cell and expound its microstructural arrangement. Fig. 1 shows the normalised unit cell of the pseudo-fractal lattice of different orders. Starting from a simple square (of order zero) and dividing it into half using the horizontal bisector two similar upper and lower rectangles are generated. The upper rectangle should then be divided using a vertical bisector. This gives rise to the first order pseudo-fractal unit cell (Fig. 1 (left)). If the aforementioned process is repeated for the upper squares, i.e. treating them as the original zeroth order rectangle, it will lead to second, third, …, and nth order pseudo-fractals.

The process explained above gives rise to the generation of the unit cell. Once the unit cell thus obtained is assigned as the basis to the points of the substratum lattice the pseudo-fractal hyper-lattice is obtained. Fig. 2(a) shows a schematic of such an arrangement while Fig. 2 (b) shows its unit cell.

Two important points must be clarified at the outset. First, it must be mentioned that the structure thus obtained contains microstructure. Thus if one wished to preserve its primary dynamic characteristics while representing it using a continuum, this could only be done using a generalized continuum theory such as the micropolar [59], micromorphic [60], Cosserat [61,62] or another generalized continuum theory. Second, the heterogeneity and anisotropy of the unit cell give rise to global anisotropy. Given the lattice constants in the two directions are the same this can be termed 'intrinsic' anisotropy and manifests itself in pseudo-fractals of the first order and above. Extrinsic anisotropy due to different directional lattice constants, on the other hand, is present even for zeroth order lattices. It is therefore essential to consider this in any continuum formulation used to simulate the problem. As for heterogeneity, macro-heterogeneity is not necessarily obtained as a consequence of micro-heterogeneity as it can be conceived that as the ratio of unit cell to lattice dimension vanishes so does heterogeneous effects and the entire medium can be assumed a homogeneous one.

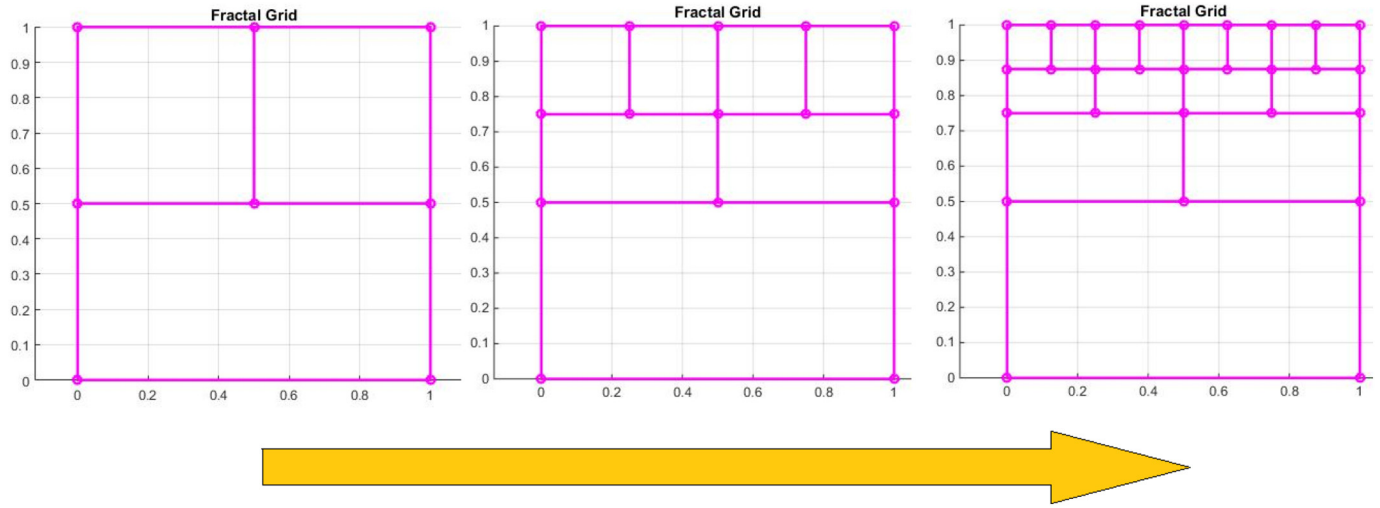

Fig. 1. Pseudo-fractal lattices in the ascending order from left to right: first order (left), second order (middle), and third order (right).

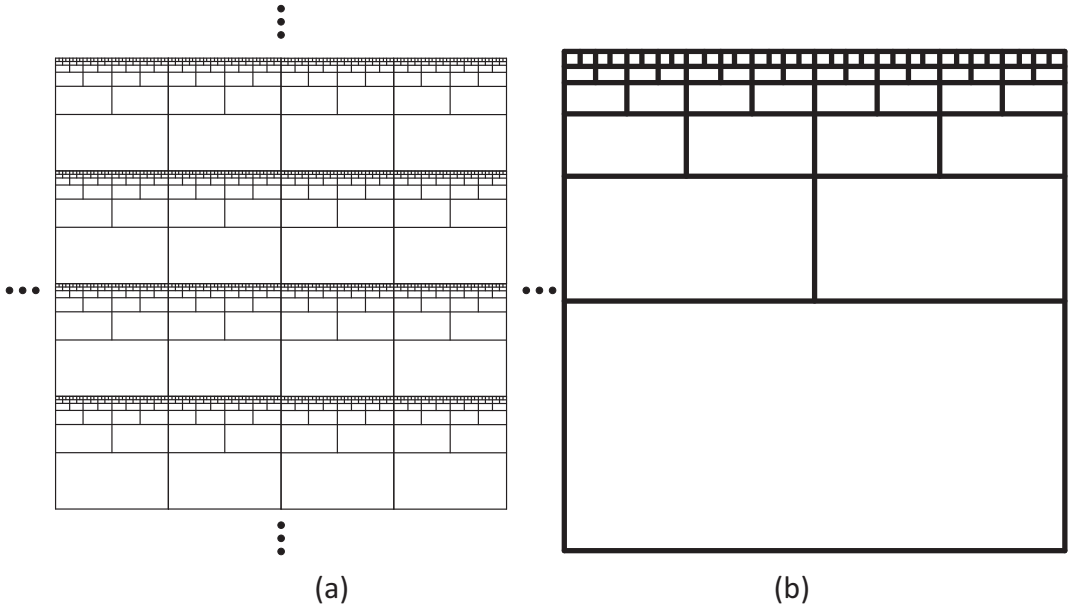

Fig. 2. (a) The schematic of a pseudo-fractal lattice of an arbitrary order, (b) the unit cell for (a).

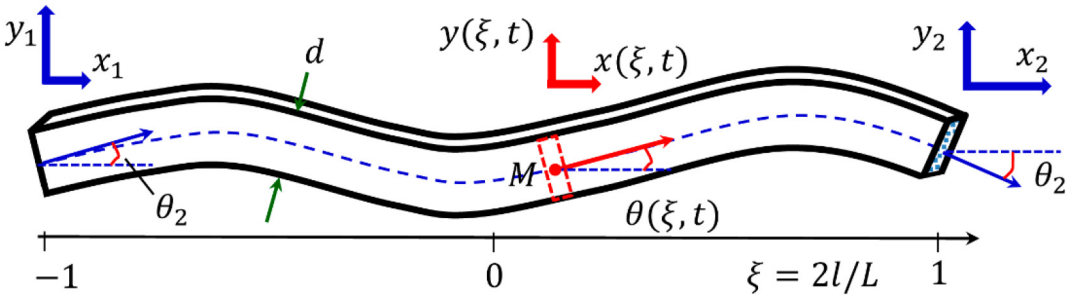

Fig. 3. The Timoshenko beam element used in the construction of the unit cell. The nodal degrees of freedom are shown by indexed letters corresponding to their displacement fields.

3. Finite element modelling of the unit cell

The unit cell of the system under consideration is a rigid-jointed network of Timoshenko beams without pre-stress. Each beam is characterized by displacements, $x_1(t), y_1(t), x_2(t), y_2(t)$, and by angles of rotation at its ends, $\theta_1(t), \theta_2(t)$ – See Fig. 3 below. Thus, a deformed state of the beam can be presented by the vector/column, $\boldsymbol{u}(t)$, with the dimensionless components

$$\boldsymbol{u}(t) = \{\hat{x}_1(t), \hat{y}_1(t), \theta_1(t), \hat{x}_2(t), \hat{y}_2(t), \theta_2(t)\}^T \tag{1}$$

where $\hat{x}_{1,2}(t) = 2x_{1,2}(t)/L$, $\hat{y}_{1,2}(t) = 2y_{1,2}(t)/L$, where L is the length of the beam.

For an arbitrary beam cross-section (marked with the letter M, see Fig. 3) the displacements and angles of rotation can be described by means of the shape-functions $a_i(\xi)$, $b_i(\xi)$, $c_i(\xi)$ and generalized coordinates $u_i(t)$:

$$\begin{aligned} x(\xi,t) &= \frac{L}{2}\sum a_i(\xi)u_i(t), \\ y(\xi,t) &= \frac{L}{2}\sum b_i(\xi)u_i(t), \\ \theta(\xi,t) &= \sum c_i(\xi)u_i(t), \quad i = 1,2,\ldots,6 \end{aligned} \tag{2}$$

where $\xi = 2l/L$, and l is measured along the axis of the beam. The shape functions are presented in Table 1.where E and G are the Young and shear modulus, respectively, $\chi = 5/6$ is the shear correction factor used in Timoshenko beam theory, and d is the width of the beam. In what follows, we shall assume $=2 \times 10^{12}$ g/(cm × s^2); $G = 8 \times 10^{11}$g/(cm × s^2); and the mass density $\rho = 7.8$ g/cm^3 (the physical parameters for steel).

Using the D'Alembert-Lagrange principle (extended Hamilton principle) we shall proceed to derive the equations of motion for the system.

Table 1

$$C = 4(1+3\beta);\ \ A = 1+3\beta;\ \ B = 1+2\beta;\ \ D = -1+6\beta; \beta = \frac{1}{12}\left(\frac{E}{\chi G}\right)\left(\frac{d}{L}\right)^2, \tag{3}$$

i	a	b	c
1	$(1-\xi)/2$	0	0
2	0	$(2A - 3B\xi + \xi^3)/C$	$(-3 + 3\xi^2)/C$
3	0	$(A - \xi - A\xi^2 + \xi^3)/C$	$(D - 2A\xi + 3\xi^2)/C$
4	$(1+\xi)/2$	0	0
5	0	$(2A + 3B\xi - \xi^3)/C$	$(3 - 3\xi^2)/C$
6	0	$(-A - \xi + A\xi^2 + \xi^3)/C$	$(D + 2A\xi + 3\xi^2)/C$

The kinetic energy of the beam per unit thickness is equal to:

$$T = \frac{1}{2}\rho d \int_{-\frac{l}{2}}^{\frac{l}{2}} \left(\dot{x}^2 + \dot{y}^2 + \frac{I}{d}\dot{\theta}^2\right) dl \tag{4}$$

where $I = I_z = d^3/12$ is the second moment (moment of inertia) of the cross-section of the beam.

Taking into account relations (2), the kinetic energy (4) can be represented as:

$$T = \frac{1}{2}\rho d\left(\frac{L}{2}\right)^3 \sum_{i=1,6}\sum_{k=1,6} \dot{u}_i \dot{u}_k T^{(ik)} \tag{5}$$

where

$$T^{(ik)} = \int_{-1}^{1} \left(a_k a_i + b_k b_i + \frac{1}{3}\left(\frac{d}{L}\right)^2 c_k c_i\right) d\xi \tag{6}$$

The potential energy of the beam equals:

$$U = \frac{1}{2}\int_{-L/2}^{L/2} Ed\left(\frac{dx}{dl}\right)^2 dl + \frac{1}{2}\int_{-L/2}^{L/2} EI_z\left(\frac{d\theta}{dl}\right)^2 dl + \frac{1}{2}\int_{-L/2}^{L/2} \chi Gd\left(\frac{dy}{dl} - \theta\right)^2 dl \tag{7}$$

which on substituting Eq. (2) into relation (7), we obtain:

$$U = \frac{1}{2}\rho d\left(\frac{L}{2}\right)^3 \left(\frac{4E}{\rho L^2}\right) \sum_{i=1,6}\sum_{k=1,6} u_i u_k U^{(ik)} \tag{8}$$

where

$$U^{(ik)} = \int_{-1}^{1} \left(a_i' a_k' + \frac{1}{3}\left(\frac{d}{L}\right)^2 c_i' c_k' + \left(\chi\frac{G}{E}\right)(b_i' - c_i)(b_k' - c_k)\right) d\xi \tag{9}$$

and where the primes denote differentiation with respect to the dimensionless axial coordinate ξ.

Thus, the Lagrangian functional ($\mathcal{L} = T(\dot{u}_i) - U(u_i)$) of the beam is equal to:

$$\mathcal{L} = \frac{1}{2}\rho d\left(\frac{L}{2}\right)^3 \sum_{i=1,6}\sum_{k=1,6} \left(\dot{u}_i \dot{u}_k T^{(ik)} - \left(\frac{4E}{\rho L^2}\right) u_i u_k U^{(ik)}\right). \tag{10}$$

The fact that the kinetic energy is a mere function of generalized velocities and not of generalized coordinates is due to the choice of Cartesian coordinates. If a general curvilinear coordinate system was chosen the kinetic energy would be a function of generalized coordinates as well as velocities. In any case the strain (potential) energy would be only a function of generalized coordinates and kinetic energy's dependence on generalized velocities is quadratic.

Strain and kinetic energy are the additive integrals of the motion. The Lagrangian functional for the unit cell, $\mathcal{L}_{cell}$, is therefore the sum of the Lagrangian functions of the single beams that constitute it. If the unit cell has an intricate structure of internal and bounding beams, then the Lagrangian functions of these (bounding) beams must be accounted for with the factor 1/2.

Below, it is convenient to operate with the displacements of the single nodes, $\hat{x}_m, \hat{y}_m, \theta_m$, contained in the unit cell ($m = 1, 2, \ldots, N$, where N is the total number of the nodes) and with the corresponding vectors are defined as:

$$\boldsymbol{v}_m = \{\hat{x}_m, \hat{y}_m, \theta_m\}^T. \tag{11}$$

The two vectors, $\boldsymbol{v}_m$ and $\boldsymbol{v}_n$, constitute the vector $\boldsymbol{u}^{(mn)} = \{\begin{smallmatrix}\boldsymbol{v_m}\\ \boldsymbol{v_n}\end{smallmatrix}\}$ that describes the dynamics of the beam connecting nodes m and n.

Thus, the system of the Euler-Lagrange equations of motion is obtained as:

$$\frac{d}{dt}\frac{\partial \mathcal{L}_{cell}}{\partial \dot{v}_{m,i}} - \frac{\partial \mathcal{L}_{cell}}{\partial v_{m,i}} = 0, i = 1,2,3; \quad m = 1,2,\ldots,N, \tag{12}$$

The equations of motion are reduced to the simple following form in the case of propagating planar harmonic waves at a frequency ω within the entire lattice:

$$-\omega^2 \boldsymbol{M}\boldsymbol{v} + \boldsymbol{K}\boldsymbol{v} = \boldsymbol{0} \tag{13}$$

where

$$\boldsymbol{v} = \{\boldsymbol{v}_1, \boldsymbol{v}_2, \ldots, \boldsymbol{v}_N\}^T, \tag{14}$$

and where **M** and **K** are the assembled global mass and stiffness matrices of the unit cell, respectively.

In accordance with Floquet-Bloch's theorem, the linear dependencies exist among the vectors $\boldsymbol{v_m}$ associated with the bounding nodes of the unit cell. If for two such l— and j—nodes the relative position, $\Delta\boldsymbol{r} = \boldsymbol{r}_l - \boldsymbol{r}_j$, is equal to a lattice translation vector, $\boldsymbol{a}$, then $\boldsymbol{v_l} = \boldsymbol{v_j}\, exp(i\boldsymbol{k}\boldsymbol{a})$, where $\boldsymbol{k}$ is the wave vector. A similar relation exists when the original position of two points is apart by an integer multiple of $\boldsymbol{a}$. Thus, the vector $\boldsymbol{v}$ can be represented in the form:

$$\boldsymbol{v} = \boldsymbol{T}(\boldsymbol{k})\hat{\boldsymbol{v}}. \tag{15}$$

The $\boldsymbol{T}(\boldsymbol{k})$-matrix size is $3N \times 3\hat{N}$, where $\hat{N}$ is the number of the linear independent vectors within the set $\{\boldsymbol{v}_1, \boldsymbol{v}_2, \ldots, \boldsymbol{v}_N\}$ that form the combined $3\hat{N}$-dimensional vector $\hat{\boldsymbol{v}}$.

Finally, the investigation of the acoustic properties of the 2D-system reduces to calculating all of the eigenvalues and eigenvectors of a generalized eigen-system as follows:

$$\omega^2\left(\boldsymbol{T}^H\boldsymbol{M}\boldsymbol{T}\right)\hat{\boldsymbol{v}} = \left(\boldsymbol{T}^H\boldsymbol{K}\boldsymbol{T}\right)\hat{\boldsymbol{v}} \tag{16}$$

where $\boldsymbol{T}^H$ is the Hermitian transposed matrix of $\boldsymbol{T}(\boldsymbol{k})$.

Below, the normalised frequency is presented in the unit of $(\frac{4E}{\rho L_0^2})^{1/2}$, where L_0 is the unit of length.

4. Analysis of the unit cell

Subsequent to imposition of periodic boundary conditions (PBC's) a unit cell could be studied for eigenfrequencies and eigenmodes. As an example, preliminary numerical studies using the Finite Element (FE) software ABAQUS were conducted on the unit cell of the first order pseudo-fractal and the schematic of the results for eigenmodes 1–12 are shown in Fig. 3.

Such studies, important as they may be, do not provide the full picture of phononic dispersion in the hyper-lattice. To gain an understanding of the morphology of dispersion surfaces as well as band structure in an infinite lattice, analytical studies using Floquet-Bloch's principle must be conducted. This principle asserts the fact that when waves without attenuation propagate in an infinite lattice created through the tessellation of repetitive identical units, the change in complex wave amplitude across a unit cell is not contingent upon the position of that cell. In other words, if the difference in the radius vectors between two points 1 and 2, $\Delta\vec{\boldsymbol{r}} = \vec{\boldsymbol{r}}_2 - \vec{\boldsymbol{r}}_1$, that are situated at the unit cell boundary is equal to some vector of the translational symmetry, then the corresponding amplitudes, $\boldsymbol{A_1}$, $\boldsymbol{A_2}$, differ from each other by only the phase factor $\boldsymbol{exp}(i\vec{\boldsymbol{k}}\Delta\vec{\boldsymbol{r}})$: $\boldsymbol{A_2} = \boldsymbol{A_1}\ \boldsymbol{exp}(i\vec{\boldsymbol{k}}\Delta\vec{\boldsymbol{r}})$, where $\vec{\boldsymbol{k}}$ is

the wave vector. Thus, one can obtain the characteristics of phononic dispersion by focusing on a unit cell (Fig. 4).

In order to obtain a unit cell one can rely on intuition or use a more systematic way of doing so as recommended by the literature [63]. Once the unit cell is transformed onto its reciprocal in the **k**-space the first Brillouin zone (BZ) is obtained. Depending on the nature of symmetries the irreducible Brillouin zone (IBZ) can be deduced which is the minimal area to be studied for phononic dispersion. If the edges of the IBZ are traversed the band structure is obtained whereas if the morphology of dispersion surfaces is of concern the area of IBZ must be taken into account.

As the full account is of interest in the present work the following section deals with the derivation of dispersion surfaces using IBZ. In the sequel we use the terms 'frequency surface' and 'dispersion surface' interchangeably.

5. Derivation of dispersion surfaces for the pseudo-fractal hyper-lattice

We embark upon our study of phononic dispersion in this class of structures under consideration by considering the simplest case of the non-fractal lattice (zeroth order pseudo-fractal hyper-lattice). The reasons are: 1) this is a suitable point of departure for the more complicated cases, 2) this provides a basis for comparison of results and the distinctive features of a hyper-lattice, and 3) the formulation will

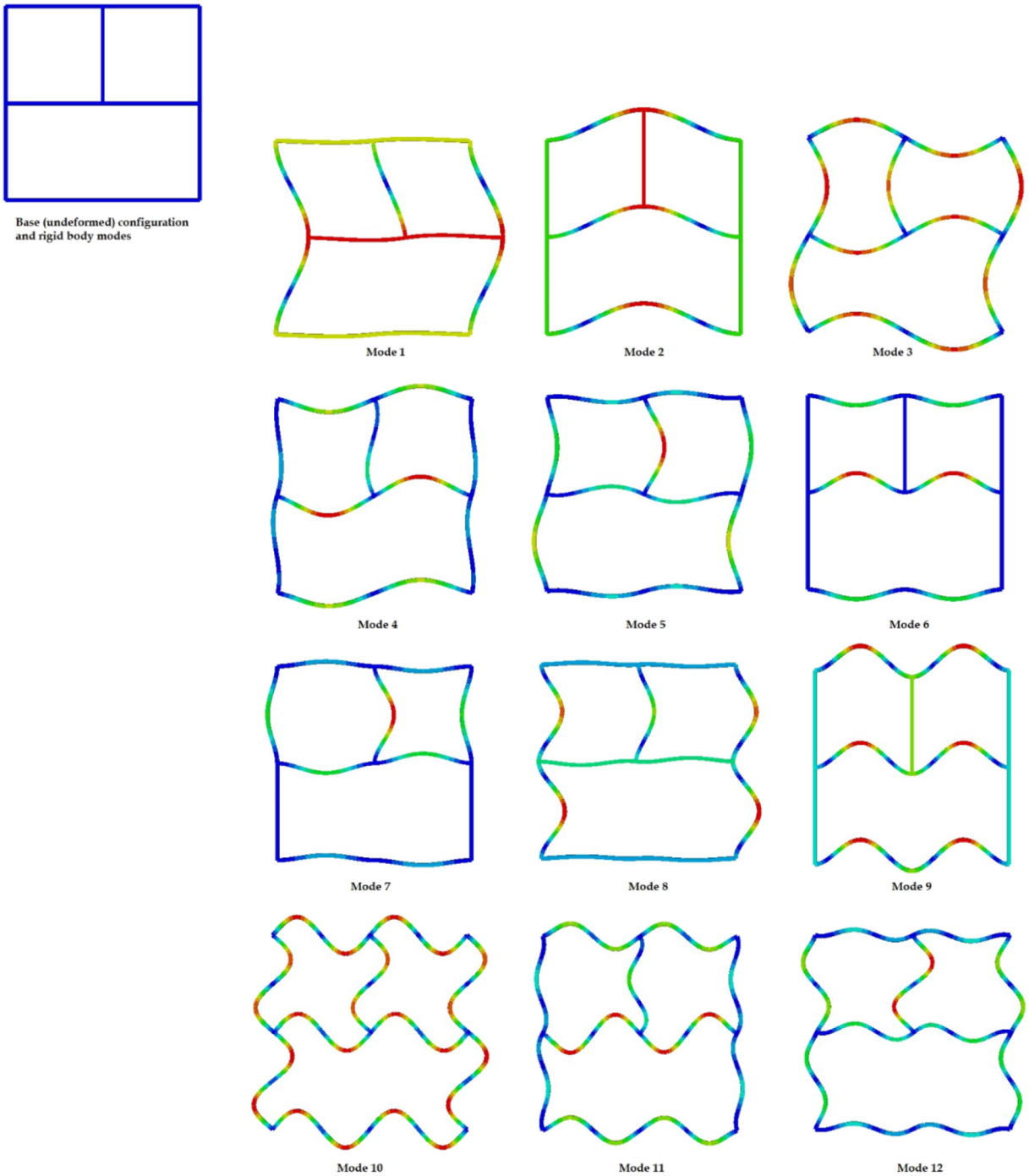

Fig. 4. The schematic of the eigenmodes for the first 12 natural modes of the unit cell in the lattice. The undeformed (initial) configuration is depicted on the upper left corner.

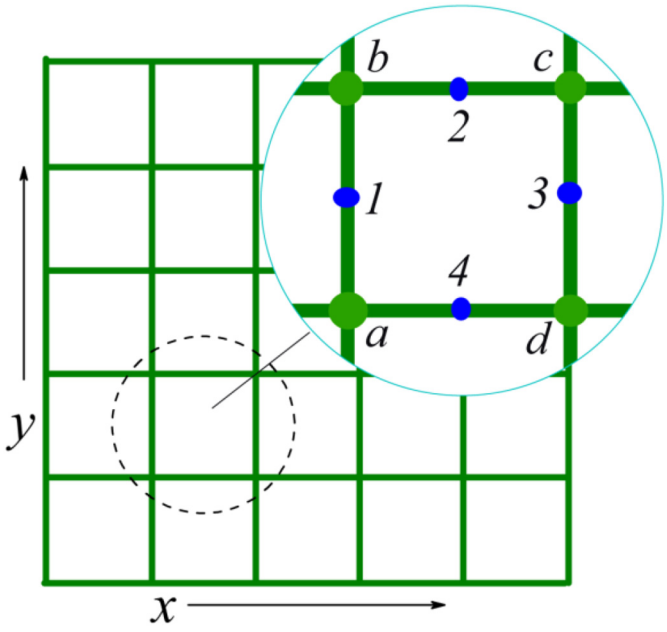

Fig. 5. The simple square lattice (zeroth order pseudo-fractal hyper-lattice).

point the way to a more comprehensive FE formulation based on pseudo-fractals.

The unit cell consists of the beams *ab*, *bc*, *cd*, *da* (see Fig. 5). If the numerical model operates only with the main nodes *a*, *b*, *c*, *d* (displacements of which are equal to $\hat{x}_p, \hat{y}_p$ and $\hat{\theta}_p$, where $\hat{\theta}_p$ is the rotation angle at the nodes $p = a, b, c, d$), then a couple of the acoustic modes and the single optical mode can be excited. The optical mode at the center of the Brillouin zone corresponds to in-phase rotations ($\hat{x}_p = 0, \hat{y}_p = 0$) of the *a*, *b*, *c*, *d* -nodes followed with S-like bends of the beams.

As a closer approximation to the real situation and in order to describe acoustic properties of the system correctly, each of the beams must be considered as a sequential assembly of *m* sub-beams which is equivalent to re-meshing in a commercial FE package. The simplest procedure to achieve this is to introduce a set of intermediate "nodes" as it is shown in Fig. 5. In this the so called 1/2-approach ($m = 2$) the corresponding system for the eight beams dynamics ($a - 1, 1 - b, b - 2, \ldots, 4 - a$) has only nine independent variables (for instance, $\hat{x}_p, \hat{y}_p, \hat{\theta}_p$ at the nodes *a*, 1 and 4). So, we can define nine dispersion $\omega(k)$-surfaces (two. acoustic modes and seven optical modes). Visually, the optical mode oscillations at $k = 0$ are shown in Fig. 6.

The twice degenerated mode A corresponds to horizontal/vertical displacements of the horizontal/vertical beams as a single entity. Simultaneously, the vertical/horizontal beams bend in anti-phase to these oscillations. Mode B was discussed above. It is the only optical mode that can be described in the simple approach without dividing the beams into a set of sub-beams. The next "new" mode C is anti-phase rotation of the intermediate nodes 1,3 relative to 2,4-nodes, when the basic nodes *a*, *b*, *c*, *d* stay motionless. The frequency of in-phase rotations of all nodes (mode D) is higher than that of the C-mode (in D-mode, the effective "wave length" of transverse bends is shorter). The twice degenerated higher mode E reminds one of the low frequency mode A but in this E-mode, opposite to A-mode, the horizontal/vertical beams move not as a single entity because of exciting the longitudinal standing wave in those modes. The first five optical surfaces are shown in Fig. 7a.

It is obvious that with increasing the parameter *m* the total number of degrees-of-freedom and frequency surfaces FS increases and is equal to $N = 3(2m - 1)$; the total number of the optical surfaces is $N_{opt} = 6m - 5$. In Fig. 7a, the five lowest optical FS-s correspond to modes A (twice degenerated), and B, C, D (Fig. 6) at $k = 0$. Apparently, these modes can also be excited at the centre of the Brillouin zone in the ¼-approach (i.e. $m = 4$). One can see identical frequency surfaces in Fig. 7b but the corresponding frequencies, $\omega_{1,\,2,\,3,\,4,\,7}(k = 0)$, are lower than these in the ½-approach (in Fig. 7a and Fig. 7b these modes are equally coloured). The reason is that the effective stiffness of the basic beams decreases with increasing the number of sub-beams and converges to the actual value. The frequency surfaces 5,6,8 in the Fig. 7b are based on the new twice degenerated mode A_2 and single mode C_2 (See Fig. 8) that are

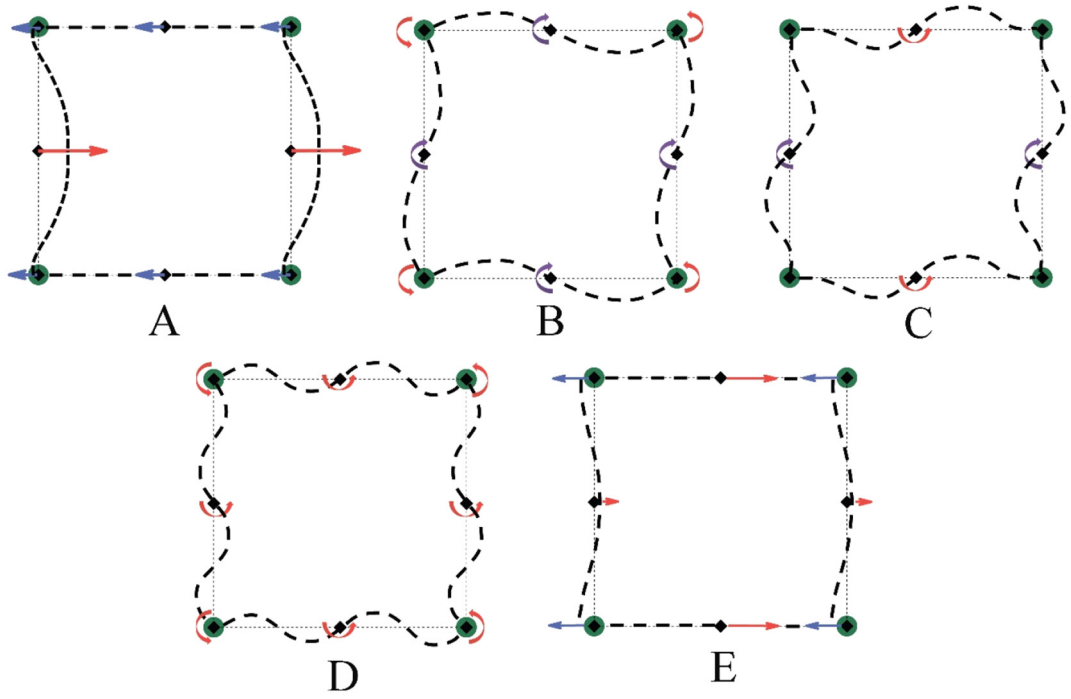

Fig. 6. Deformations of the unit cells if the optical modes are excited (results of the numerical model). Both the A- and E-types of oscillations are twice degenerated at $k = 0$ because these modes can be oriented along X- and Y-axes identically (only X-polarization is shown there).

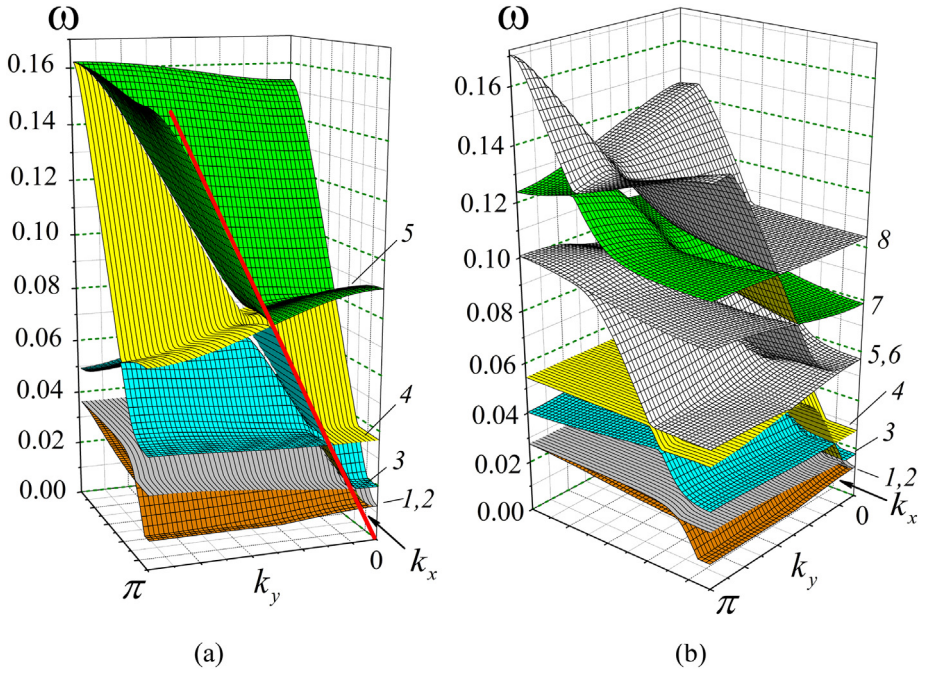

Fig. 7. The lower optical frequency surfaces for $m = 2$ (A) and $m = 4$ (B). $N_{opt}(m = 2) = 7$ and $N_{opt}(m = 4) = 19$. In the Fig. 7a, the two upper optical frequency surfaces based on the twice degenerated mode E (See Fig. 6) are not shown.

higher frequency analogies to modes A and C, correspondingly (See Fig. 6). This wedging-in of the additional mode between the previously existing modes results in the appearance of classical analogy to the quantum energy levels repulsion. This repulsion flattens the frequency surfaces, which is especially displayed by the flattening of the 4th and 5th surfaces (yellow, green in Fig. 7a) when the parameter m increases (Fig. 7b).

In both the 1/2 - and 1/4 –approach the sets of the frequency-surfaces (See Fig. 7) look like a result of intersections of some acoustic modes (ω~k; see the red line in Fig. 7a) with relatively flat optical modes, which are followed with breaking up these surfaces at the zone of the intersection as the result of the level repulsion mentioned above (See [20] for a full account of such phenomena). Neighboring surfaces can touch each other only at single points.

Increasing the parameter m (by satisfying the inequality $L/m \gg d$) results in a closer approach to the real spectrum of oscillation (discrete at any wave vector $\boldsymbol{k}$) with the highest frequency growing. However, as one can see in Fig. 9, frequency gaps appear at high frequency area and there are frequency surfaces that have the same frequency pass band. Moreover, the square lattice is a rather symmetrical structure, which gives rise to many rotation modes (See, for instance, B,C,D-modes in Fig. 6 and C_2-mode in Fig. 7) without (or almost without)

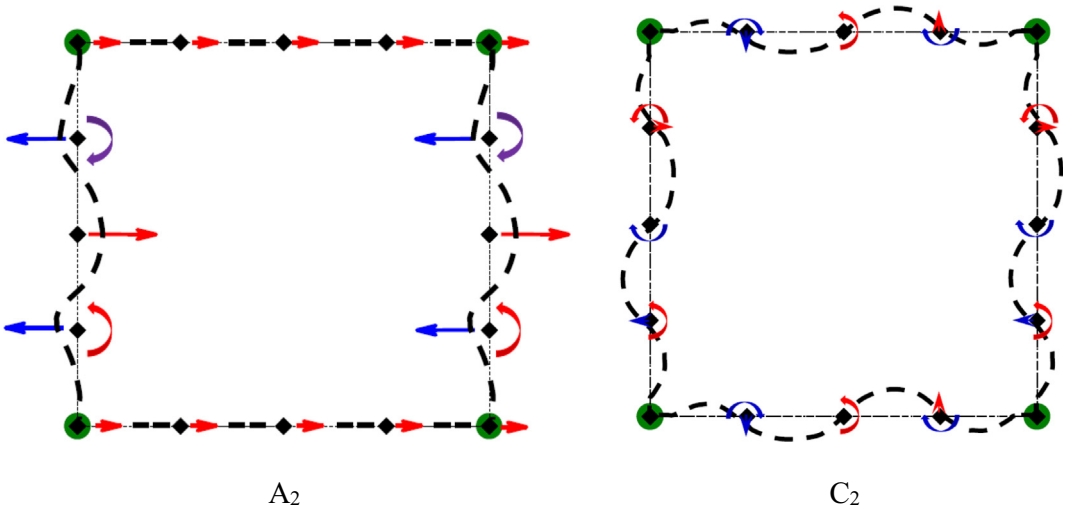

Fig. 8. The examples of characteristic deformations of the unit cell at $k = 0$ that appear in the ¼- approach and are not observed in the ½- approach. The A2- and C2-modes are analogous to modes A and C shown in Fig. 6 but with the higher frequency order (lower "wavelength" for the transverse basic beam oscillations).

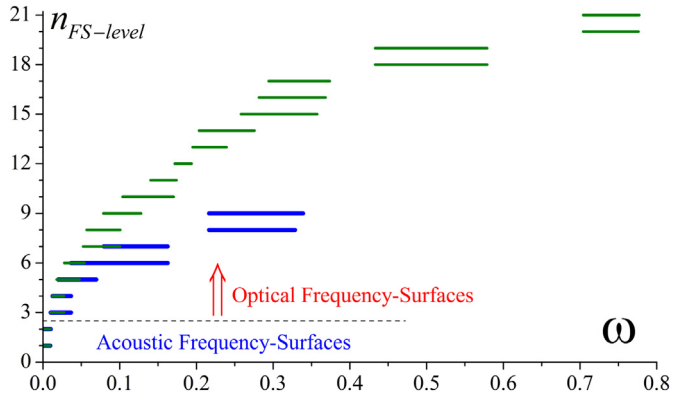

Fig. 9. The frequencies pass bands spectra in the 1/2-approach se (blue) and 1/4- approach (olive). The length of the basic beams, *L*, is equal to 8, the width, *d*, equals 0.2. For each frequency-surface the pass band $\omega_{min} \le \omega \le \omega_{max}$ is marked with the corresponding horizontal length.

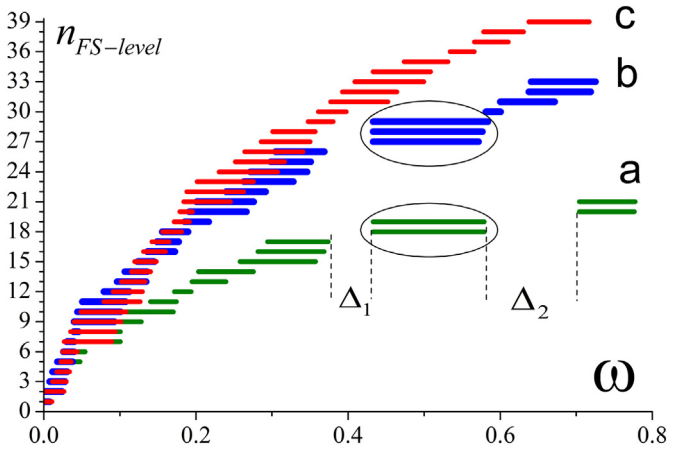

Fig. 11. The pass bands spectra in the 1/4- approach. The results for the initial square lattice (a-olive) shown in Fig. 9, for the pseudo-fractal structures of type I (b-blue), there are 33 frequency surfaces and for type II (c-red) 39 frequency surfaces.

displacements of the main nodes of the lattice. These modes dominate at $k = 0$ (see the frequency-surfaces 8 in Fig. 7b, for instance) and are hard to be excited. Thus, the square lattice is not an appropriate system when regarded as an element of detectability e.g. a sensitive sensor.

More promising are the structural arrangements which are non-symmetrical fractal-like (pseudo-fractal) lattices based on square units – See Fig. 10.

where $\boldsymbol{n_{FS-level}}$ is the number of frequency surfaces, $\boldsymbol{\omega} = \boldsymbol{\omega_n}(\vec{\boldsymbol{k}})$, assigned in the ascending order, $\boldsymbol{\omega_{n+1}}(\vec{\boldsymbol{k}} = \boldsymbol{0}) \ge \boldsymbol{\omega_n}(\vec{\boldsymbol{k}} = \boldsymbol{0})$, $\boldsymbol{n} = \boldsymbol{1}, \boldsymbol{2}, \boldsymbol{3}, \ldots \boldsymbol{3\hat{N}}$. The structure of the type I (Fig. 11, the spectrum b) eliminates the gap Δ_2 but retains the gap Δ_1 and does not split the identical frequency pass bands marked with ellipses in Fig. 11. The structure of the type II removes both the undesirable frequency band gaps, Δ_1, Δ_2, and the overlapping/degenerate frequency pass bands.

It is obvious that with shortening the sub-beams to the length of *L*/8 the total pass band extends. Moreover, there is the possibility of using the pseudo-fractal structure of the next order of complexity-See. Figs. 12, and 13. The higher the total number of the frequency-surfaces the more densely these surfaces cover some defined frequency interval. For instance, the frequency band Δ (Fig. 13) is covered with six surfaces in the case of type-II structure but with twelve surfaces in the case of type-III pseudo-fractal structure.

It must be noted that in Fig. 12 the red dots merely denote geometric points and not particles of mass.

One can see the almost "flat" frequency-surfaces with narrow pass band, $\Delta\omega_n = \omega_{n,\,max} - \omega_{n,\,min}$, as well as with relative wide pass band ($\Delta\omega_n$~0.1) like the one shown in Fig. 14.

The morphology of the frequency-surfaces reflects the inhomogeneity of the system under consideration. This is the intrinsic inhomogeneity to which we have alluded in a previous section. In the areas of high frequencies the corresponding frequency-surfaces rather extensively in the X-direction but minimally in the Y-direction (see Fig. 12 and 14b).

The B,C,D-modes in Fig. 6 and C_2-mode in the Fig. 8 can be classified as rotation modes in contradistinction to the A and E-modes in Fig. 6 (for instance). In a general case, every independent eigen column vector $\hat{\boldsymbol{v}}$, which is the solution of Eq. (16) and is represented by $3\hat{N}$ components

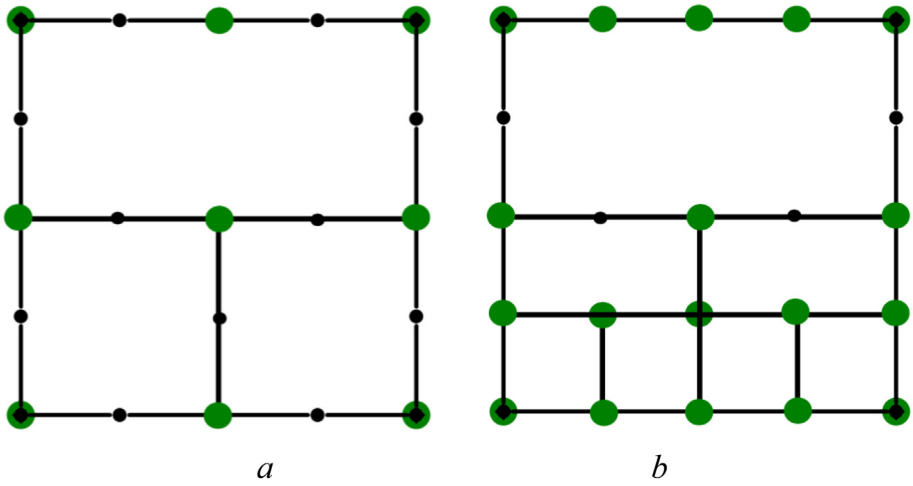

Fig. 10. The unit cells in like-fractal structures of the type I (a) and II (b) based on 1/4- approach (the size of smallest square is in four time less than the size of the unit cell, *L*). Olive circles – the lattice nodes, black points – the lattice sub-nodes.

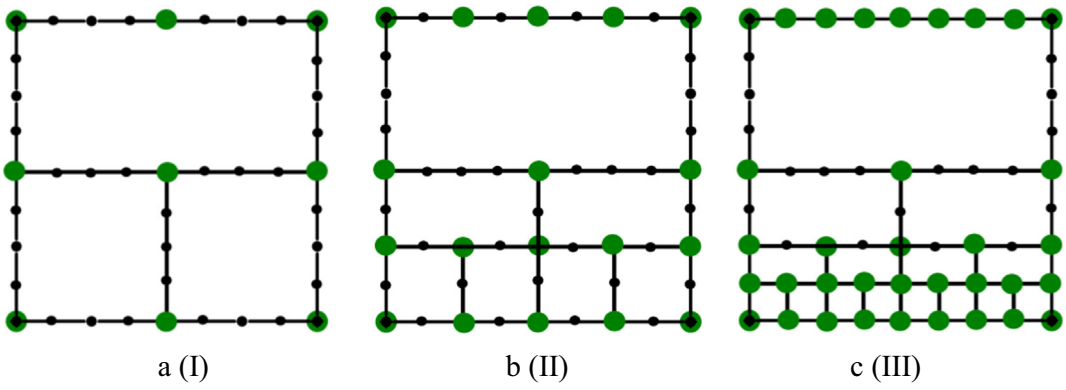

Fig. 12. The 1/8-unit cells in like-fractal structures of type I (a), II (b), and III(c).

(see Eqs. (11), (14), and (15)), may be characterized with the value:

$$\gamma = \hat{\boldsymbol{v}}^T \cdot \hat{\boldsymbol{v}} - \sum_{i=3,6,9,\ldots,3\hat{N}} (\hat{v}_i)^2 \equiv 1 - \sum_{i=3,6,9,\ldots,3\hat{N}} (\hat{v}_i)^2. \quad (17)$$

where the sum $\sum_{i=3,6,9,\ldots,3\hat{N}} (\hat{v}_i)^2$ describes the partial contribution of the nodal rotations, when interpreting the type of oscillations corresponding to the column vector $\hat{\boldsymbol{v}}$. The low values of parameter γ, mean the oscillations are rather 'rotating' than 'displacing' and vice versa.

The ratio L/d greatly influences the types of vibrations in the pseudo-fractal structures – See. Fig. 15. There, the parameter $\langle\gamma_n\rangle$ is averaged over each of the n—frequency-surfaces and the value of $\gamma(\boldsymbol{k})$ is defined by Eq. (17).

6. Conclusions

We may now summarise the results obtained. It has been established as a fact that the higher frequencies that can be exited in the simple square lattice (Fig. 5) are almost the same compared to those in the pseudo-fractal structures (as the comparison between the Fig.'s 10,12 and Fig.'s 11,13 shows) independent of the approach adopted (i.e. the number, m, of sub-beams). However, with increasing the order of pseudo-fractal structure (tailorability) the number of degrees-of-freedom increases. As a result, increasing the frequency surfaces number (i) eliminates the frequency gaps (Fig. 9), which can be useful for acoustic/phononic visibility/detectability e.g. in designing a sensor, (ii) the classical analogy of the quantum level repulsion flattens the frequency-surfaces which sufficiently decreases the sound group velocity in the pseudo-fractal structure, and can be used for practical applications [64–66]. For instance, the average value of the frequency pass-bands of the single optical modes, $\langle\Delta\omega_n\rangle$, and its corresponding standard deviation, $\delta(\Delta\omega_n)$, are equal to 0.047 and 0.030, respectively for type I pseudo-fractal of Fig. 12, and 0.033 and 0.019 for type III pseudo-fractal (Fig. 12). Especially low group wave velocities can be reached along Y-direction (See Fig. 14).

Finally, an important feature of the pseudo-fractal acoustic wave spectrum must be discussed. In the simple square lattice the single "rotating" modes alternate with the single "displacing" modes when the frequency increases (Fig. 7b). In the pseudo-fractal hyper-lattice structure the rotating modes can be extracted to the separate wide frequency area – Fig. 15b. Thus, a wide frequency-gap for the displacing modes emerges that works simultaneously as the pass-band for rotating modes. Conversely, there are two (lower and upper) frequency areas that are non-transparent for the rotating modes (Fig. 15b).

While pseudo-fractal hyper-lattices can be designed with relative ease and through an iterative procedure they exhibit unique features unattainable by ordinary lattice design. They also provide the designer with enough freedom to allow for the design of a light-weight sensor with alterable pass- and stop- bands.

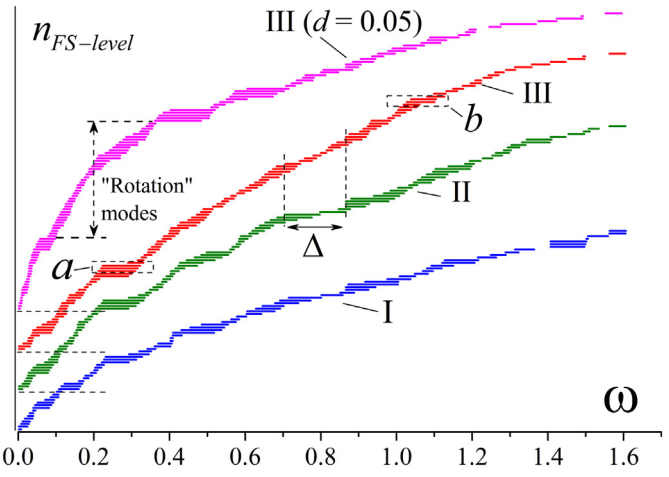

Fig. 13. The pass bands spectra for the pseudo-fractal structures of the type I (75 FS's), II (99 FS's), and III (111 FS's) shown in Fig. 12. To avoid overlapping these diagrams, they are shifted along the vertical axis. The geometrical parameters are $L = 8$, $d = 0.2$. The upper spectrum is the result for $d = 0.05$; i.e. the ratio of the length of the shortest sub-beam to its width is equal to 5 (for most cases) and 20 in the single case of structure III, respectively.

Data availability statement

The raw/processed data required to reproduce these findings cannot be shared at this time as the data also forms part of an ongoing study.

Contribution of authors

The original idea was proposed by A S Fallah and V N Gorshkov.

N Navadeh and A S Fallah derived the equations for the FE beam model.

V Tereshchuk and V N Gorshkov ran simulations and derived dispersion surfaces.

All authors contributed to writing the paper.

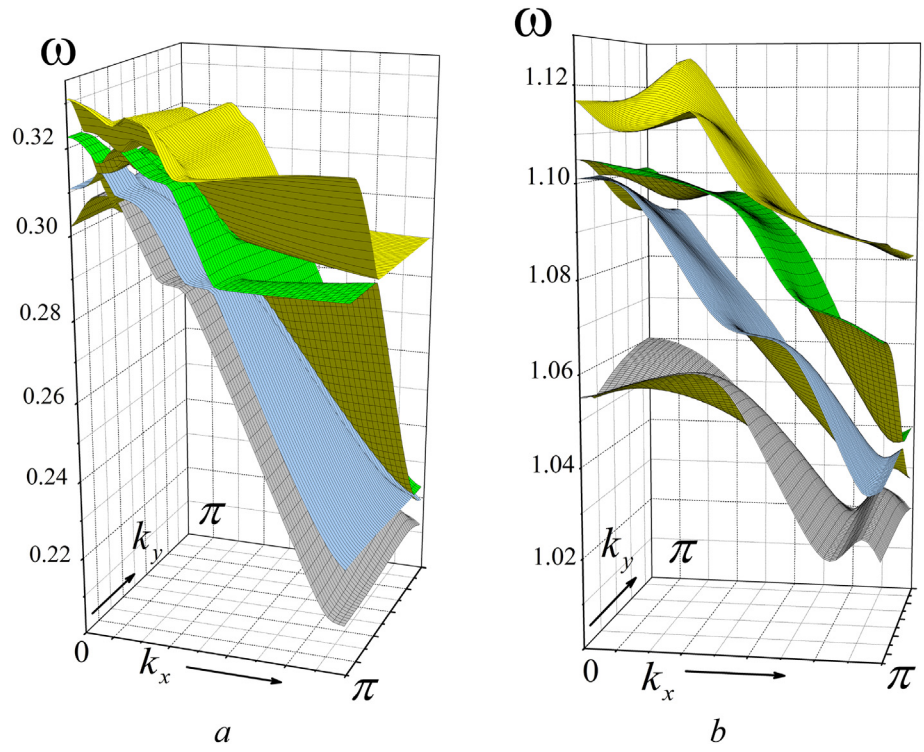

Fig. 14. Examples of the frequency surfaces in type-III structure a – for the frequency surfaces included to the area marked with the a-rectangular in Fig. 13; b - for the frequency surfaces of the b-rectangular in Fig. 13.

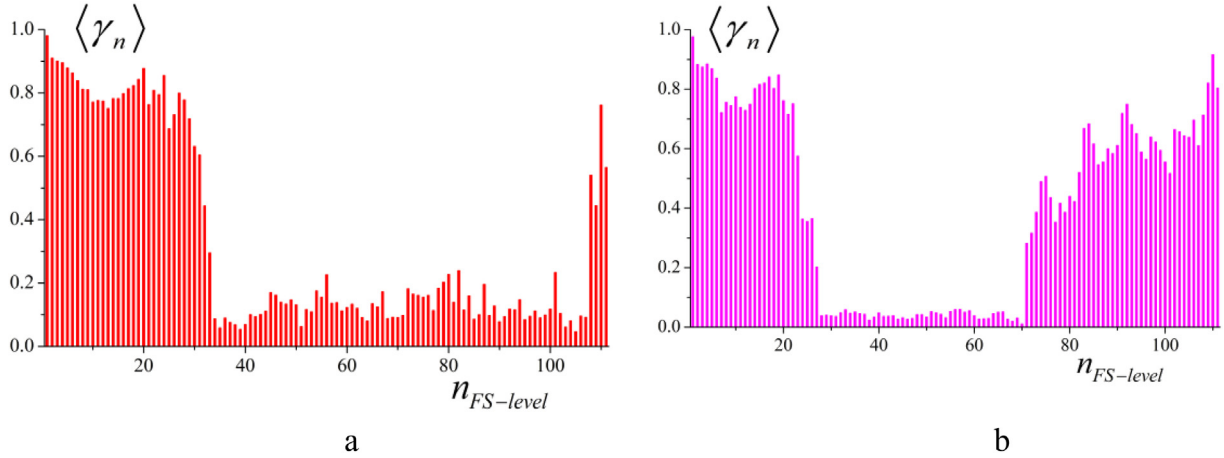

Fig. 15. Splitting the modes of vibration (frequency surfaces) into the rotation mode group (low $\langle \gamma_n \rangle$) and the displacing modes ($\langle \gamma_n \rangle \geq 0.2$). Results for the 1/8—type III pseudo-fractal structures presented in Fig. 13. $L = 8$, $d = 0.2$ (a) and $d = 0.05$ (b). The rotation modes in the case shown in Fig. 15b ($\langle \gamma_n \rangle \ll 1$) are denoted in Fig. 13 – See the upper diagram.

References

[1] B. Mandelbrot, How long is the coast of Britain? Statistical self-similarity and fractional dimension, Science 156 (3775) (1967) 636–638.
[2] B. Mandelbrot, Fractals, Freeman, San Francisco, 1977 24.
[3] M.F. Barnsley, Fractals everywhere, Academic Press, 2014.
[4] B.B. Mandelbrot, Fractal aspects of the iteration of z → Λz (1-z) for complex Λ and z, Ann. N. Y. Acad. Sci. 357 (1) (1980) 249–259.
[5] N. Cohen, Fractal antenna applications in wireless telecommunications, Electronics Industries Forum of New England, 1997, Professional Program Proceedings 1997, May, pp. 43–49, (IEEE).
[6] R.G. Hohlfeld, N. Cohen, Self-similarity and the geometric requirements for frequency independence in antennae, Fractals 7 (01) (1999) 79–84.
[7] J.L. Véhel, E. Lutton, C. Tricot, Fractals in Engineering: From Theory to Industrial Applications, Springer Science & Business Media, 2012.
[8] E. Domany, S. Alexander, D. Bensimon, L.P. Kadanoff, Solutions to the Schrödinger equation on some fractal lattices, Phys. Rev. B 28 (6) (1983) 3110.
[9] C. Puente-Baliarda, J. Romeu, R. Pous, A. Cardama, On the behavior of the Sierpinski multiband fractal antenna, IEEE Trans. Antennas Propag. 46 (4) (1998) 517–524.
[10] C.P. Baliarda, J. Romeu, A. Cardama, The Koch monopole: a small fractal antenna, IEEE Trans. Antennas Propag. 48 (11) (2000) 1773–1781.
[11] G. Kron, Tensor Analysis of Networks, J. Wiley & Sons, 1939.
[12] G. Kron, Tensorial analysis of integrated transmission systems part i. the six basic reference frames, Trans. Am. Inst. Electr. Eng. 70 (2) (1951) 1239–1248.
[13] L. Brillouin, Wave Propagation in Periodic Structures: Electric Filters and Crystal Lattices, Courier Corporation, 2003.
[14] A.S. Phani, J. Woodhouse, N.A. Fleck, Wave propagation in two-dimensional periodic lattices, J. Acoust. Soc. Am. 119 (4) (2006) 1995–2005.
[15] S. Gonella, M. Ruzzene, Analysis of in-plane wave propagation in hexagonal and re-entrant lattices, J. Sound Vib. 312 (1–2) (2008) 125–139.
[16] E.N. Economou, M.M. Sigalas, Classical wave propagation in periodic structures: cermet versus network topology, Phys. Rev. B 48 (18) (1993) 13434.
[17] Y. Yang, A.S. Fallah, L.A. Louca, Frequency analysis of a heterogeneous perforated panel using a super-element formulation, J. Sound Vib. 327 (1–2) (2009) 26–40.
[18] H.H. Huang, C.T. Sun, G.L. Huang, On the negative effective mass density in acoustic metamaterials, Int. J. Eng. Sci. 47 (4) (2009) 610–617.
[19] H.H. Huang, C.T. Sun, Wave attenuation mechanism in an acoustic metamaterial with negative effective mass density, New J. Phys. 11 (1) (2009) 013003.

[20] V.N. Gorshkov, N. Navadeh, A.S. Fallah, A study of frequency band structure in two-dimensional homogeneous anisotropic phononic K3-metamaterials, Smart Mater. Struct. 26 (9) (2017) 095058.
[21] X.N. Liu, G.K. Hu, G.L. Huang, C.T. Sun, An elastic metamaterial with simultaneously negative mass density and bulk modulus, Appl. Phys. Lett. 98 (25) (2011) 251907.
[22] A.S. Fallah, Y. Yang, R. Ward, M. Tootkaboni, R. Brambleby, A. Louhghalam, L.A. Louca, Wave propagation in two-dimensional anisotropic acoustic metamaterials of K4 topology, Wave Motion 58 (2015) 101–116.
[23] V.N. Gorshkov, N. Navadeh, P. Sareh, V.V. Tereshchuk, A.S. Fallah, Sonic metamaterials: reflection on the role of topology on dispersion surface morphology, Mater. Des. 132 (2017) 44–56.
[24] X. An, H. Fan, C. Zhang, Elastic wave and vibration bandgaps in two-dimensional acoustic metamaterials with resonators and disorders, Wave Motion 80 (2018) 69–81.
[25] M. Dekking, J. Lévy-Véhel, E. Lutton, C. Tricot, Fractals: Theory and Applications in Engineering: Theory and Applications in Engineering, Springer Science & Business Media, 2012.
[26] J. Ding, L. Fan, S.Y. Zhang, H. Zhang, W.W. Yu, Simultaneous realization of slow and fast acoustic waves using a fractal structure of Koch curve, Sci. Rep. 8 (1) (2018) 1481.
[27] G.Y. Song, B. Huang, H.Y. Dong, Q. Cheng, T.J. Cui, Broadband focusing acoustic lens based on fractal metamaterials, Sci. Rep. 6 (2016) 35929.
[28] R.C. Norris, J.S. Hamel, P. Nadeau, Phononic band gap crystals with periodic fractal inclusions: theoretical study using numerical analysis, J. Appl. Phys. 103 (10) (2008) 104908.
[29] G. Ma, P. Sheng, Acoustic metamaterials: from local resonances to broad horizons, Sci. Adv. 2 (2) (2016) e1501595.
[30] X. Zhu, K. Li, P. Zhang, J. Zhu, J. Zhang, C. Tian, S. Liu, Implementation of dispersion-free slow acoustic wave propagation and phase engineering with helical-structured metamaterials, Nat. Commun. 7 (2016) 11731.
[31] Y. Cheng, C. Zhou, B.G. Yuan, D.J. Wu, Q. Wei, X.J. Liu, Ultra-sparse metasurface for high reflection of low-frequency sound based on artificial Mie resonances, Nat. Mater. 14 (10) (2015) 1013.
[32] X. Zhu, B. Liang, W. Kan, Y. Peng, J. Cheng, Deep-subwavelength-scale directional sensing based on highly localized dipolar mie resonances, Physical Review Applied 5 (5) (2016) 054015.
[33] G.Y. Song, Q. Cheng, B. Huang, H.Y. Dong, T.J. Cui, Broadband fractal acoustic metamaterials for low-frequency sound attenuation, Appl. Phys. Lett. 109 (13) (2016) 131901.
[34] J. Liu, L. Li, B. Xia, X. Man, Fractal labyrinthine acoustic metamaterial in planar lattices, Int. J. Solids Struct. 132 (2018) 20–30.
[35] W.L. Chen, G.M. Wang, Effective design of novel compact fractal-shaped microstrip coupled-line bandpass filters for suppression of the second harmonic, IEEE Microwave Wireless Compon. Lett. 19 (2) (2009) 74–76.
[36] C. Borja Borau, G. Font, S. Blanch Boris, J. Romeu Robert, High directivity fractal boundary microstrip patch antenna, Electron. Lett. 36 (9) (2000) 778–779.
[37] J. Anguera, C. Puente, C. Borja, R. Montero, J. Soler, Small and high-directivity bow-tie patch antenna based on the Sierpinski fractal, Microw. Opt. Technol. Lett. 31 (3) (2001) 239–241.
[38] C.T.P. Song, P.S. Hall, H. Ghafouri-Shiraz, D. Wake, Sierpinski monopole antenna with controlled band spacing and input impedance, Electron. Lett. 35 (13) (1999) 1036–1037.
[39] T. Cai, G.M. Wang, J.F. Zhao, M. Yao, Two-dimensional fractal metasurface and its application to low profile circularly polarized antennas, Journal of Electromagnetic Waves and Applications 29 (3) (2015) 410–423.
[40] J. McVay, N. Engheta, A. Hoorfar, High impedance metamaterial surfaces using Hilbert-curve inclusions, IEEE Microwave Wireless Compon. Lett. 14 (3) (2004) 130–132.
[41] J. Christensen, F.J.G. de Abajo, Anisotropic metamaterials for full control of acoustic waves, Phys. Rev. Lett. 108 (12) (2012) 124301.
[42] Z. Liang, J. Li, Extreme acoustic metamaterial by coiling up space, Phys. Rev. Lett. 108 (11) (2012) 114301.
[43] Y. Li, X. Jiang, R.Q. Li, B. Liang, X.Y. Zou, L.L. Yin, J.C. Cheng, Experimental realization of full control of reflected waves with subwavelength acoustic metasurfaces, Physical Review Applied 2 (6) (2014) 064002.
[44] Y. Xie, W. Wang, H. Chen, A. Konneker, B.I. Popa, S.A. Cummer, Wavefront modulation and subwavelength diffractive acoustics with an acoustic metasurface, Nat. Commun. 5 (2014) 5553.
[45] S. Castiñeira-Ibáñez, C. Rubio, V. Romero-García, J.V. Sánchez-Pérez, L.M. García-Raffi, Design, manufacture and characterization of an acoustic barrier made of multi-phenomena cylindrical scatterers arranged in a fractal-based geometry, Archives of Acoustics 37 (4) (2012) 455–462.
[46] T. Frenzel, J. David Brehm, T. Bückmann, R. Schittny, M. Kadic, M. Wegener, Three-dimensional labyrinthine acoustic metamaterials, Appl. Phys. Lett. 103 (6) (2013) 061907.
[47] W. Wen, L. Zhou, J. Li, W. Ge, C.T. Chan, P. Sheng, Subwavelength photonic band gaps from planar fractals, Phys. Rev. Lett. 89 (22) (2002) 223901.
[48] D. Chen, S. Wang, L. Li, Z. Liu, X.Z. Zhao, M. Zhang, Z. Chen, Microstrip filter with H-shaped fractal, Appl. Phys. Lett. 88 (25) (2006) 253507.
[49] F. Miyamaru, Y. Saito, M.W. Takeda, B. Hou, L. Liu, W. Wen, P. Sheng, Terahertz electric response of fractal metamaterial structures, Phys. Rev. B 77 (4) (2008) 045124.
[50] B. Hou, H. Xie, W. Wen, P. Sheng, Three-dimensional metallic fractals and their photonic crystal characteristics, Phys. Rev. B 77 (12) (2008) 125113.
[51] M. Dupré, F. Lemoult, M. Fink, G. Lerosey, Exploiting spatiotemporal degrees of freedom for far-field subwavelength focusing using time reversal in fractals, Phys. Rev. B 93 (18) (2016) 180201.
[52] N.K. Kuo, G. Piazza, Fractal phononic crystals in aluminum nitride: An approach to ultra high frequency bandgaps, Appl. Phys. Lett. 99 (16) (2011) 163501.
[53] X. Liu, Y. Fan, Y. An, The influence of T-square fractal shape holes on the band structure of two-dimensional phononic crystals, Phys. B Condens. Matter 429 (2013) 73–78.
[54] Q.J. Lim, P. Wang, S.J.A. Koh, E.H. Khoo, K. Bertoldi, Wave propagation in fractal-inspired self-similar beam lattices, Appl. Phys. Lett. 107 (22) (2015) 221911.
[55] Y. Chen, L. Wang, Tunable band gaps in bio-inspired periodic composites with nacre-like microstructure, J. Appl. Phys. 116 (6) (2014) 063506.
[56] Y. Chen, L. Wang, Multiband wave filtering and waveguiding in bio-inspired hierarchical composites, Extreme Mech. Lett. 5 (2015) 18–24.
[57] P. Zhang, A.C. To, Broadband wave filtering of bioinspired hierarchical phononic crystal, Appl. Phys. Lett. 102 (12) (2013) 121910.
[58] D. Mousanezhad, S. Babaee, R. Ghosh, E. Mahdi, K. Bertoldi, A. Vaziri, Honeycomb phononic crystals with self-similar hierarchy, Phys. Rev. B 92 (10) (2015) 104304.
[59] J. Dyszlewicz, Micropolar Theory of Elasticity, Vol. 15, Springer Science & Business Media, 2012.
[60] A.C. Eringen, Mechanics of micromorphic continua, Mechanics of generalized continua, Springer, Berlin, Heidelberg 1968, pp. 18–35.
[61] R.D. Mindlin, Stress functions for a Cosserat continuum, Int. J. Solids Struct. 1 (3) (1965) 265–271.
[62] S.C. Cowin, Stress functions for Cosserat elasticity, Int. J. Solids Struct. 6 (4) (1970) 389–398.
[63] C. Kittel, Introduction to Solid State Physics, vol. 8, Wiley, New York, 1976.
[64] P.L. Marston, Negative group velocity Lamb waves on plates and applications to the scattering of sound by shells, J. Acoust. Soc. Am. 113 (5) (2003) 2659–2662.
[65] G.M. Gehring, A. Schweinsberg, C. Barsi, N. Kostinski, R.W. Boyd, Observation of backward pulse propagation through a medium with a negative group velocity, Science 312 (5775) (2006) 895–897.
[66] H. Lamb, On group-velocity, Proc. Lond. Math. Soc. 2 (1) (1904) 473–479.